# Molecular Design of Dispersed Nickel Phthalocyanine@Nanocarbon Hybrid Catalyst for Active and Stable Electroreduction of CO$_2$

Zisheng Zhang[a, +], Yang-Gang Wang[a*]

[a] Department of Chemistry, Southern University of Science and Technology, Shenzhen 518055, China

Abstract

The molecular catalyst/nanocarbon hybrid through $\pi - \pi$ stacking immobilization is an emerging family of single-atom catalysts with outstanding performance in electrocatalysis, well-defined active site, and tunability at molecular level through functional group substitution. In the present work, we provide a general strategy for the rational design of molecular single-atom catalyst in the form of Nickel Phthalocyanine@Nanocarbon for highly efficient electroreduction of CO_2 to CO. We employ density functional theory (DFT) calculations and state-of-the-art electronic structure analysis to explore the mechanism and substituent effects on structural stability, redox chemistry, adsorption properties and molecule-substrate interactions of the NiPc catalyst. We have revealed that the electron-withdrawing groups facilitate the reductive activation of the catalytic Ni center but weakens the Ni-N bond strength and make the CO desorption sluggish, while the electron-donating groups do the opposite. A substituent-dependent correlation between interaction strength and electron transfer through the interface is also revealed by non-covalent interaction analysis and electron density difference projection. Based on the gained insights, we apply semiempirical quantum mechanical (SQM) calculation, machine learning (ML), and genetic algorithm (GA) to screening through the chemical space of c.a. 10 trillion substituted NiPc molecules under a descriptor scheme to identify promising molecular candidates for the NiPc@NC hybrid material. The best candidate from GA search outperforms the state-of-the-art catalyst in terms of stability, reduction potential (improved by 100mV), and interaction with substrate (strengthened by 0.46 eV). Designing strategies are proposed based on the top-scoring molecules from computational screening, and the workflow is highly generalizable and transferable to similar molecular systems for other applications.

TOC Graphic
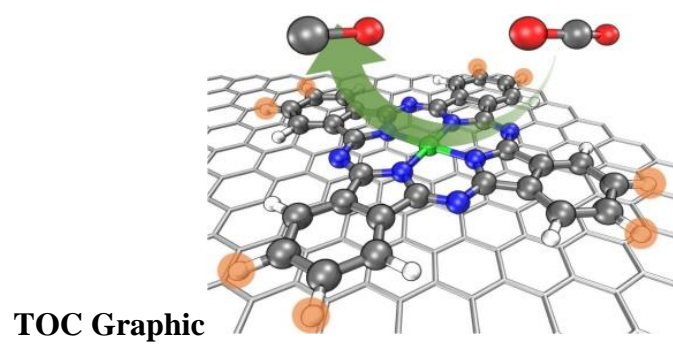
Introduction

The climbing carbon emission worldwide has been intensifying the Greenhouse Effect which poses threat on ecosystems and causes extreme weather condition over the globe.[1] It is more than crucial for humanity to develop a sustainable and environmental-friendly energy infrastructure which can properly close the carbon cycle of ecosystem. CO_2 reduction reaction (CO_2RR) is the most straightforward and scalable way to convert carbon dioxide into value-added chemicals using surplus renewable energy, hence one of the most promising technologies in the field of environmental and energy science.[2] The gaseous product of such reaction, including CO, CH_4, C_2H_4 etc., can be easily separated from the reaction system and are important building blocks of chemical industry and pharmaceutics.[3] However, few electrocatalyst, other than noble metal-based materials (e.g., Pt, Au, IrO_2, and RuO_2), can meet the demand of practical application in terms of kinetics, selectivity and stability.[3,4] Therefore, it is critical to develop electrocatalysts based on earth-abundant transition metals (TM) with performance comparable to that of noble metals.

In the recent decade, single atom catalyst (SAC) is a rapidly growing hot spot in electrocatalysis.[5–7] By embedding transition metal atoms into conducting matrix such as nanostructured carbon materials, the electrocatalysts can achieve atomic dispersion which not only drastically boosts the atomic efficiency but also provides a platform for mechanistic study utilizing operando characterization techniques.[8–11] However, those SAC are usually derived from pyrolysis of carbon-containing precursor or wet impregnation method, which usually suffers from sintering of metal atoms into clusters or nanoparticles (that requires additional removal step).[12] Moreover, it is rather difficult to fine-tune the local electronic structure since there is not exact control of doping position in the preparation process.

In terms of atomic level understanding of the active site and manipulatable local environment, molecular systems, especially transition metal phthalocyanines and porphins, could outperform SACs since their geometric and electronic structures are more well-defined,[13,14] hence one can make modifications to it by substituent or through-space effects based on understanding of the electronic structure-activity relationship to improve

its property towards a certain optimum, i.e. molecular engineering.[15–18] The concept has been widely applied to various energy application including solar cell,[19] redox flow cell,[20] molecular photocatalysis,[21] and homogeneous electrocatalysis.[22–24] In the recent decade, with the development of low-cost quantum mechanical methods, researchers are able to simulate over large molecular libraries by high-throughput virtual screening.[25] The low-cost quantum mechanical methods or predictive machine learning (ML) models, when coupled with a proper molecular representation and evolutionary algorithms, make extremely efficient possible optimization of a certain molecular property in any predefined chemical subspace, with minimal human interference.[26]

Although there has been exciting progress in rational or inverse design of molecular electrocatalysts, due to sluggish charge transfer kinetics with the electrode, efforts have been made to immobilize molecular electrocatalysts onto electric conducting substrate to achieve heterogenization.[27,28] This family of heterogeneous molecular catalysts, also featuring atomically dispersed active sites, have been accepted as a member of the SAC.[29,30] However, many studies adopt covalent immobilization approaches which may introduce structural changes to the molecular catalysts. To avoid such effect, immobilization through non-covalent π-π stacking is one of the most successful techniques to anchor macrocyclic metal complex on heterogeneous conducting carbon substrate. In 2017, Liang and coworkers reported the non-covalent immobilization of molecularly engineered cobalt phthalocyanine (CoPc) onto carbon nanotubes (CNTs) via π-π stacking to achieve 98% Faradic Efficiency (FE) towards selective CO_2RR to CO with superior activity.[31] Moreover, the non-covalent interaction it utilizes to achieve immobilization prevents the supported metal complex from structural changes, allowing preservation of the molecular integrity and fine-tuning of the electronic structure of the SA sites at atomic scale. In our recent work, rational designed NiPc-OMe@CNT hybrid achieved unit conversion to CO with high current density, and the tetramethoxy substitution improves the stability of NiPc which suffers from deactivation in its pristine form.[32] Recently, Liu and coworkers also demonstrated that NiPc-NH$_2$@CNT to be an efficient and selective electrocatalysis for electrochemical reduction of CO_2 to CO.[33] The combined multiscale engineering approach provide a clear and efficient strategy towards

rational design of SAC for electrocatalytic applications, and emerges as a promising platform for experimental and computational studies of electrocatalytic mechanisms.

In this study, we focus on the NiPc for CO_2RR since its reaction pathway is not altered after substitution of even strong electron-withdrawing groups (EWG) and electron-donating groups (EDG), unlike CoPc which branches into CH_4 pathway when EDG is introduced.[34] The reaction mechanism of CO_2RR to CO on NiPc is discussed with density functional theory (DFT) calculation. The bonding mode and interaction between adsorbate and nickel center are investigated in depth with extensive wavefunction analysis and energy decomposition analysis. After understanding the molecular system, we take a few steps further into the realistic realm to evaluate the effect of interaction between NiPc and the nanocarbon substrate and the through-space electron transfer across the $\pi - \pi$ stacking interface. Based on the understandings, we performed computational screening combining genetic algorithm (GA), semiempirical quantum mechanical (SQM) calculation, and deep neural network (NN) model to explore the chemical space of substituted nickel phthalocyanines. The top-scoring candidate molecules are reported, and several design strategies are concluded from the computational screening.

Methods

The CO₂RR is studied under the computational hydrogen electrode (CHE) scheme[35] where the electron and proton transfer steps are treated as coupled, and the zero voltage is defined based on the reversible hydrogen electrode under standard condition. The effect of applied bias on a proton-electron transfer step is represented by adding a $-eU$ term to the standard ΔG. The CO₂RR pathways are listed below (* stands for the active site):

$$(1)\ *CO_2 + H^+ + e^- \rightarrow *COOH$$

$$(2)\ *COOH + H^+ + e^- \rightarrow *CO + H_2O$$

$$(3)\ *CO \rightarrow * + CO$$
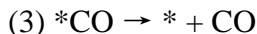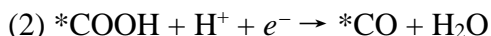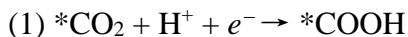
DFT calculations on isolated molecules (nickel phthalocyanines, H_2, H_2O, CO_2 and CO) are performed using the Gaussian 16 program, A.03 edition.[36] PBE0 functional[37] with D3 correction (Becke-Johnson damping)[38] is adopted for its robustness and dispersion corrections which make it widely accepted as proper functional to study reaction energetics of transition metal complexes. The Stuttgart-Dresden (SDD) basis set, containing all double-ξ valence with effective core potentials (ECPs), is employed for transition metal atoms (Ni).[39] For all other main group elements (H, C, N, O), the all-electron 6-31G* basis set[40–42] was used. Harmonic vibrational frequencies were computed to make sure that all reaction intermediates have no imaginary frequency. The Gibbs free energies are calculated with the harmonic potential approximation at optimized structures at 298.15 K and 1 atm. Solvation free energies are calculated by the implicit SMD model[43] with M05-2X functional[44] and 6-31G* basis set, which is the level of theory where the SMD is parameterized against experimental datasets,[45] with water being the solvent.

MO analysis, generalized charge decomposition analysis, non-covalent interaction analysis, and electrostatic potential mapping are performed using the Multiwfn program on the previously obtained wavefunctions from DFT calculation.[46] Symmetry-adapted perturbation theory (SAPT)[47] calculations with restricted open-shell Hatree Fock (ROHF) reference are performed using PSI4 package[48] to decompose the interaction between the

two fragments into components of physical meaning. For better description of weak interactions while reducing the computational cost, aug-cc-pVDZ basis set is used for Ni, cc-pVDZ for H and jun-cc-pVDZ for all other elements.[49]

The geometric optimization, adsorption energy, and charge density of NiPc molecules supported on nanocarbon substrate are computed using the CP2K simulation package for its capability of efficiently computing relatively large systems (~400 atoms in this case).[50] The spin-polarized PBE exchange-correlation functional was adopted with double-zeta Gaussian basis sets for describing the valence electrons[51] and an auxiliary plane-wave basis set with a cutoff of 400 Ry for computing the electrostatic terms.[52] D3 correction is included to better describe the dispersion interaction. The nanocarbon substrate was modeled by a 12×12 graphene monolayer on which the NiPc molecule was placed in a face-to-face manner. A vacuum slab with thickness of 20 Å was added to eliminate the fictitious interaction in the z-direction. Note that although the electronic structure of our employed model may deviate from CNT, a 1:1 model would be too computational demanding (>2200 atoms for a 2 nm long fragment of CNT with 3 nm radius) otherwise.[53] Model of CNT with size reduced to affordable range or a bent graphene would cause severer errors than this study due to too small curvature or spurious interactions.[54] In addition, the π-π stacking energy has been shown to rely more on proper formulation of the dispersion term and the geometry than exact description of the band structures.[55] Hence, main conclusions obtained with our model could translate to graphene, pyrolyzed graphitic carbon, and the outer wall of CNTs with small curvature.

SQM calculations are performed using the xTB package.[56] GFN2-xTB tight binding method is employed in this study for its low computational cost on large systems and comparable accuracy to DFT methods in geometry optimization, noncovalent interaction, and MO energy calculation.[57] Since periodic GFN2-xTB is not yet implemented, the nanocarbon substrate is modeled by a 8×8 hexagonal graphene molecule cut out from monolayer graphene with terminal C atoms saturated with hydrogen.

In the computational screening section, each molecule is represented by a 1D vector with 42 (number of substituents) × 8 (number of substitution sites) binary elements via positional one-hot encoding. The representation can reversibly interconvert into or from a

SMILES representation.[58] The SMILES string is converted to XYZ coordinate using Open Babel package,[59] and sufficient stochastic conformational search is performed at MMFF94 level to obtain the most stable conformation.[60]

In the genetic algorithm search, each one-hot encoded representation acts as a gene. Based on the calculated descriptors, a fitness factor is assigned to each candidate. Mating rates are assigned according to the fitness, and the child inherits 50% of the gene from each of its parents randomly. Mutations are introduced by choosing a substitution site and replace the substituent on it randomly. The mutation rate is set at 33% to ensure sufficient sampling of the chemical subspace and avoid being trapped into local minima. When the population size exceeds the limit of 100 candidates, the candidates with the lowest fitness are removed. GA run is regarded as converged when the fittest candidate remains in the pool for 50 generations.

The machine learning model for fast prediction of molecular properties is a deep neural network (NN) with four rectified linear unit (ReLU) activated hidden linear layers. The NN is trained on the dataset of randomly sampled substituted NiPc, with 80% of the data as training set and 20% of the data as test set. Data augmentation is achieved by rotating the molecule to generate 4 equivalent representations for each data point. The validity of the machine learning model on the subspace that the current population is located is evaluated every 10 generations by calculating the R square between the NN-predicted value and the QM value. The NN is employed until the R square drops below 0.9, after which the level of theory is switched to SQM methods in the following generations.

Result & Discussion

CO₂ Electroreduction on NiPc Molecules with Different Substitutes. Previous experimental reports have shown that NiPc molecule needs to go through two reduction steps before it can catalyze CO₂RR, as evidenced by the two reduction peaks prior to the reduction current in cyclovoltammetry, both in case of free-standing NiPc and NiPc/CNT hybrids.[32,61] Such finding makes the mechanistic studies based on the neutral NiPc molecule problematic since the electronic structure of the Ni center can change greatly after the reduction process. In addition, since the standard reduction potential of CO₂RR to CO (-0.10 V vs. RHE in water) is more positive than the reduction potential of NiPc molecule, the onset potential of the reaction is likely to be dependent on the reductive activation of the NiPc itself instead of the barriers of the electrocatalytic process. For example, the energy profile of CO₂RR on neutral NiPc calculated under the computational electrode (CHE) scheme and with implicit solvation model predicts a prohibitively high overpotential of over 1.1 V (**Figure 1a**), which deviate from experimental values greatly. It is hence crucial to resolve the entity of the NiPc after reductive activation. There are earlier reports proposing the stepwise NiPc → [NiPc]⁻ → [NiPc]²⁻ mechanism, however, it is unlikely because the reductive activation is also observed on NiPc/CNT, in which case negatively charged cathode would naturally repel the NiPc away if it were reduced to anion, which contradicts the absence of Ni content in the electrolyte after electrolysis by ICP-MS in ref [32]. Therefore, all intermediate forms of NiPc should have zero net charge. In addition, the N atoms bridging between the isoindole units in NiPc gain a ~3 times larger negative charge compared to the Ni center supposing it gains an extra electron to form [NiPc]⁻ (**Figure S1a, S1b**), making the N sites easy subject to protonation in the neutral aqueous media. In our recent work, we combined DFT calculation and operando XAS to reveal the molecular structure of the intermediate structures (Figure 1b).[62] The reduction of NiPc is in fact coupled with protonation of the Pc ligand, and two such protonation steps are needed to activate the NiPc into NiPc-2H species for CO₂RR. The free energy change for attaching H to the Pc ligand has been calculated to be 0.32 eV, 0.54 eV, and 0.49 eV on NiPc-CN, NiPc-OMe, and unsubstituted NiPc, respectively. EWG can lower the protonation energy by depleting the electron density over the ligand and lowering the LUMO energy level to

facilitate the reduction of the Pc ligand that precedes the protonation, while the EDG does the opposite job. The trend is consistent with the experimental reduction potential and the calculated LUMO energy levels with R^2 values of 0.9896 and 0.9944, respectively. The *operando* XANES showed the gradual distortion and decomposition of the Ni-N$_4$ unit due to Ni loss in the unstable NiPc@CNT and NiPc-CN@CNT catalysts, which contradicts the formation and repelling of [NiPc]$^{2-}$ species which would instead result in a fading pattern without distortion. The *operando* EXAFS result is also consistent with the fitting based on the DFT-optimized NiPc-2H geometry, featuring two different Ni-C patterns (symmetry change from D$_{4v}$ to D$_{2v}$ upon protonation), and the same goes for the adsorbate configuration *CO. The energy profile of CO$_2$RR is recalculated on the protonated forms under the CHE scheme, and the predicted overpotential is reduced to 0.59 V. Although the overpotential of CO$_2$RR calculated from CHE is not a good indicator of actual reactivity since the onset is limited by the reduction activation of NiPc, it still suggests the radical change of electronic structure and energetics on NiPc-2H since the geometries of *CO and *COOH on NiPc-2H (**Figure 1d**) does not differ much from those on neutral NiPc. It should be noted that the CHE calculation on gas phase geometry with implicit solvation is a crude approximation to the physical reality where the carbon substrate and explicitly water molecules can play some role in modulating the electronic structure of the molecule and stabilization of the reaction intermediates.[63]

To evaluate the effect on the NiPc by introducing substituents, we further calculated the NiPc with tetramethoxy- substitution and with octacyano- substitution, denoted as NiPc-OMe and NiPc-CN, respectively. The -OMe and -CN substituents are chosen for availability of experimental data and that they belong to the one of strongest EDG and EWG, respectively. Little deviation from the geometries of intermediates on neutral forms are observed, evidencing the consistent reaction pathway of the three NiPc molecules. The HOMO (highest occupied molecular orbital), LUMO (lowest unoccupied molecular orbital), LUMO+1 (LUMO and LUMO+1 are degenerate MOs), and LUMO+2, together with their energy levels are summarized in **Figure S2**. It is apparent that the HOMO and LUMO are mainly contributed by ligand, and a more rigorous orbital composition analysis reveals the contribution of Ni to be ~0% for HOMO and ~1% for LUMO, indicating Pc as the redox center. The ligand-centered redox chemistry is

consistent with previous *operando* XANES report where the oxidation state of Ni (+II) is almost unchanged when the potential is increased from open-circuit voltage to the potential of stable operation.[32] It is also supported by the electron density map in **Figure S1a** where the absolute majority of the extra electron are located on the ligand and that there is only a minor decrease in Ni Mulliken charge by ~0.02 and a minor weakening of Ni-N Mayer bond order by ~0.05 upon formation of NiPc-2H species. Introduction of EDG upshifts the MO energy levels, making it harder to reduce, while EWG would do the opposite job. By comparing the LUMO energies with experimental reduction potential of the second activation steps (-0.22 V for NiPc-CN, -0.64 V for NiPc, -0.69 V for NiPc-OMe),[32] it is obvious that a lower LUMO energy leads to a less negative reduction potential for activation, hence an earlier onset. Furthermore, there exists a linear correlation between the reduction potential and LUMO energy level with R square of 0.9993 (**Figure S3**), which is consistent with the linear relationships between DFT-calculated MO energy and redox potential that have been reported on similar molecular systems.[64–66] Therefore, LUMO energy level could act as a decent descriptor for predicting the reduction potential of the activation process. The LUMO+2 is an anti-bonding orbital for all four Ni-N bonds in Ni-N_4 moiety, the filling of which at high overpotential is likely to substantially weaken the Ni-N bonds and lead to structural distortion and even Ni-N cleavage. Therefore, from a MO perspective, introduction of EDG does help prevent the breakage of the Ni-N_4 moiety by upshifting the energy level of anti-bonding LUMO+2 out of reach.

For the neutral NiPc species, CO_2RR exhibits no pronounced difference in energetics among the three molecules (**Figure 1a**). However, in their activated form, the energetics of the reaction intermediates on three molecules differ. It can be seen in **Figure 1c** that the energy of *COOH is in order of NiPc-CN-2H > NiPc-2H > NiPc-OMe-2H, while the energy of *CO is in order of NiPc-OMe-2H > NiPc-2H > NiPc-CN-2H. Despite the fact that the electrochemical barriers are not well described under CHE scheme due to dependence of onset on reduction of the NiPc itself, the energy difference between intermediates on different molecules are worthy of discussion, since ΔG (change in Gibbs free energy) is not as reliable a metric as $\Delta\Delta G$ (change in ΔG upon changing substituents), especially for the thermodynamic CO desorption process. The *CO adsorption strength is

calculated to be NiPc-CN > NiPc > NiPc-OMe, which contradicts with the conventional view that a more electron-rich center should bind CO stronger due to enhanced back-donation. In contrast, orbital interaction diagram from generalized charge decomposition analysis (GCDA) shows that there is no back donation in the NiPc-2H*CO intermediate (**Figure 2a**). The π and π^* orbitals of CO have little interaction with NiPc-2H MOs, and the CO π^* orbital is two MOs beyond the LUMO of NiPc-2H*CO, eliminating the presence of back-donation from Ni d orbital to CO π^* orbital. The adsorption of CO on Ni in NiPc-2H*CO is therefore mainly contributed by CO σ orbital. As can be seen in **Figure 2a**, the σ orbital of CO interacts with the metal-centered MO a_g and the ligand-centered MO b_{1u} of NiPc-2H to form MO $1a_1$, $2a_1$, and $3a_1$ in the NiPc-2H*CO complex. MO $1a_1$, $2a_1$, and $3a_1$ are all occupied and far below the frontier orbitals. In terms of Ni-C bond by σ-donation of CO to Ni, two of the three orbitals are bonding orbitals while one is anti-bonding. The Mayer bond order of Ni-C is calculated to be 0.52, which is significantly lower than the typical Ni-C coordination bond by σ-donation (the Ni-C in Ni(CO)$_4$ has a Mayer bond order of 1.03).

The electron transfer from CO to Ni is visualized by the electron density difference map between the fragments (NiPc-2H and CO) and the complex (NiPc-2H*CO). From **Figure 2b**, it can be found that the electron density shifts from O to C, forming Ni-C bond through σ-donation. The injected electron density from CO mostly goes into the $d_z{}^2$ orbital, while the electron density at the Ni-N bond region is reduced caused by structural distortion and polarization, leading to weakening of the Ni-N bond as is evidence by decrease of Mayer bond order from 0.56 in NiPc-2H to 0.46 in NiPc-2H*CO. The electron transfer number from CO to Ni-N$_4$ calculated by GCDA, as labeled below the electron density difference plot in **Figure 2b**, are 0.22 |e|, 0.20 |e|, and 0.19 |e| for NiPc-CN-2H, NiPc-2H, and NiPc-OMe-2H, respectively. The smaller electron transfer number is, the weaker interaction there is between the two fragments. The relationship can well explain the sequence of CO desorption energy of NiPc-CN-2H > NiPc-2H > NiPc-OMe-2H. The adsorption energy trend and Ni-N weakening upon CO adsorption also provides evidence for the experimental long-term stability of NiPc-OMe > NiPc > NiPc-CN, since

the deactivation is mainly caused by poisoning of the active site by CO and loss of the Ni from Ni-N$_4$ breakage.

Having evaluated the bonding interactions, we further analyzed the non-covalent interactions (NCI) involved in the NiPc-2H and its *COOH and *CO intermediates. **Figure 3** shows the reduced density gradient (RDG) plot of NiPc-2H*CO and NiPc-2H*COOH. In **Figure 3a**, four red spikes can be observed between C in CO and the four N in Ni-N$_4$ moiety, which correspond to the repulsive non-covalent interaction arising from the nonbonded overlap of electron density of C and the conjugate system over the Ni-N$_4$ moiety. Therefore, a more electron-rich Ni center would weaken the adsorption of CO. In **Figure 3b**, besides the similar red surfaces between C and Ni, green RDG surfaces can be observed between the two O in *COOH and the center of the protonated ring in the Pc ligand, which suggests slightly attractive van der Waals interaction. It is also worth noting that the protonated N-H moiety in NiPc-2H can be stabilized by the two beta C-H through a moderate attractive van der Walls interaction (Figure 3c). In addition, the steric bulk of nearby isoindole units could also prevent the N-H from getting deprotonated by solvent molecules under weak oxidative potentials. For NiPc with a smaller electron density over the ring (by EWG functionalization), such stabilization effect would be weaker. This could explain why the CV of NiPc-CN@CNT is somewhat reversible while that of NiPc-OMe@CNT is not in ref [32].

Since the weak interactions are shown to be present and may plays a crucial role in the energetic of *CO and *COOH intermediates by NCI analysis, we calculated the electrostatic potential (ESP) of the NiPc-OMe, NiPc, NiPc-CN (**Figure 4a-c**), and their activated species (**Figure 4d-f**) and mapped the ESP on their van der Waals surface. The ESP on Ni-N4 moieties of all molecules share the same shape: one maximum above the Ni center, four minima above each of the four N atoms, and four maxima above each of the center of the 6-member rings. EDG and EWG results in a more negative or a more positive ESP at the Ni-N$_4$ moiety, respectively. After the reductively activation, the maxima at Ni and minima at N of all three molecules shifts to a more negative value. The substituent effect still holds in the activated species. It is worth noting that the protonation breaks the D$_{4h}$ symmetry of the electronic structure at Ni-N$_4$ moiety, leading

14

to a relatively more positive ESP over the center of the protonated ring. To study the interaction between the activated molecules and the adsorbates, we also calculated the ESP of CO and COOH fragments. **Figure 4g** shows that the ESP minima on the CO surface lies at the C side, while the plane that intercepts the C=O has positive ESP. The ESP isosurfaces of CO (**Figure 4i**) indicates the presence of a lone pair at the C side, which supports the σ-donation bonding mode in Ni-N and causes the repulsion between C in CO and N in Ni-N. As for COOH fragment, two ESP minima are located near the two O atoms, and the H terminal of the -OH has an ESP maximum (**Figure 4h**). ESP isosurfaces of COOH fragment reveals that the two ESP minima arise from the lone pairs of O atoms, and their docking with the relatively positive maxima on protonated ring of activated NiPc molecules likely give rise to the attractive van der Waals interaction shown in **Figure 3b**. The C side at which COOH binds Ni, however, has positive ESP. In summary, the C sites in CO and COOH fragments have different ESP, resulting in different energy trends when bonded to the Ni-N$_4$ moiety.

To gain more detailed insights into the complex interaction between Ni-N$_4$ and adsorbent (CO, COOH), symmetry-adapted perturbation theory (SAPT) calculations with restricted open-shell Hatree Fock (ROHF) reference are performed to decompose the interaction between the two fragments into components of physical meaning. The decomposed energy components, together with the total SAPT energy, are summarized in **Table 1**. The total SAPT energy of *CO intermediates follow the sequence of NiPc-CN-2H*CO < NiPc-2H*CO < NiPc-OMe-2H*CO, which is consistent with the DFT calculation. It can be seen that the interaction between Ni-N$_4$ and CO is dominated by repulsive exchange interaction, i.e. Pauli repulsion, between CO σ orbital and the π orbital over electron-rich Ni-N$_4$ region after reduction as evidenced in **Figure 3a**. However, in the case of *COOH, the pronounced difference of induction energy among the three species makes induction energy the dominating contributor to the difference between three substituted NiPc molecules. Due to the positive atomic charge of C in COOH as evidenced in **Figure 4j**, a more electron-rich Ni center would result in a stronger induction interaction between Ni and C in *COOH. This can be also supported by the atomic charge calculated by modified Mulliken atom population defined by Bickelhaupt, which is 0.92, 0.87, and 0.86 for NiPc-CN-2H, NiPc-2H, and NiPc-OMe-2H, respectively. Therefore, when EDG is

introduced to the NiPc, the Ni-N$_4$ moiety becomes more electron-rich, resulting in strengthened COOH binding while weakened CO binding.

Molecular Catalyst/Support Interaction. The diverse adsorption properties induced by molecular engineering inspires us to look further into other factors that may be in effect in the realistic electrocatalytic system. Although the supported NiPc on nanocarbon (NC) substrate can preserve its structure and well-defined Ni-N$_4$ center, the interaction between NiPc molecules and NC could vary for different substituents. In operation, the electrons driven by applied potential move from electrode to NC and then transfer to the supported NiPc molecule via through-space electron transfer across the π-π stacking interface. In addition, strong enough π-π stacking interaction is a prerequisite of the hybrid system since the NiPc needs to be immobilized on NC in a stable way. Therefore, the molecular catalyst/support interaction is worth exploration.

In the DFT calculation, the NC substrate is modeled a sufficiently large periodic graphene monolayer. Due to relatively large radius of CNT (20~30 nm) compared to size of NiPc molecule (< 1 nm), the curvature of graphitic carbon layer at the interface is negligible. Therefore, the graphene monolayer model can also act as an affordable approximation to the CNT surface. The geometries are optimized at PBE-D3 with double-zeta gaussian-planewave basis set to obtain the $\pi - \pi$ stacking geometry.

The adsorption energies (E_{ads}) of NiPc, NiPc-CN, and NiPc-OMe on graphene is calculated to evaluate the strength of interaction between them. The E_{ads} are -2.47 eV, -2.88 eV, and -3.52 eV for NiPc, NiPc-OMe, and NiPc-CN, respectively. The strengths of adsorption are in order of NiPc-CN > NiPc-OMe > NiPc, which surprisingly does not fit into the EDG/EWG-tuning context which would predict either NiPc-OMe > NiPc > NiPc-CN or NiPc-CN > NiPc > NiPc-OMe. To gain deeper understanding of the interaction, NCI analysis is performed on the three hybrid structures to visualize the noncovalent interaction between the graphene and NiPc molecules (**Figure 5**). All three NiPc molecules are about 3.2 Angstrom from the graphene surface, and the RDG surface at the interface in between is colored in a mixture of green and brown, suggesting the nature of $\pi - \pi$ stacking to be mainly attractive van der Waals interaction. The surface between the main body of the Pc ligand and the graphene are very similar among the

three hybrids, however, the regions below the substituents differ greatly. The terminal H at the pristine NiPc has little interaction with the graphene (**Figure 5b**), however, the cyano groups in NiPc-CN (**Figure 5a**) and methoxy groups in NiPc-OMe (**Figure 5c**) extends the RDG surface, meaning additional attractive contribution. Therefore, the $\pi -$ π stacking is not directly reliant on the electron push-pull effects of the substituents but depends more on the polarizability of the substituent fragment (for enhanced dispersion interaction) and whether the substituent contains pi MOs to extend the conjugated system of the Pc ligand (for expanded interaction region). From the previously calculated ESP map in **Figure 4**, it can be seen that the charge redistribution is much more pronounced (evidenced by more extreme ESP values) on NiPc-CN and NiPc-OMe compared to NiPc. The dependence of $\pi - \pi$ stacking strength on nature of the substituents is consistent with previous reports on substituted aromatic molecules.[67]

Since the interaction between NiPc molecules and graphene are pure $\pi - \pi$ stacking without any chemical bond, a stronger interaction between them should give rise to stronger coupling of the electronic structure and hence facilitated electron transfer and transport, which is of grave importance in the electrocatalytic process but is often neglected in computational studies. Here we apply a surface charging technique to investigate the effect of substituents on the electron transfer at the interface. To be specific, one additional electron is added to the graphene to model the negatively charged NC surface, and the neutral NiPc molecule is attached to the charged surface, and the negatively charged hybrid is relaxed to its local minimum. By subtracting the electron density of the charged graphene substrate and the neutral NiPc from the charged hybrid, the electron transfer to NiPc can be visualized by the electron density difference map. Since the number of extra electrons added to the graphene substrate is the same among the three hybrids, the driving force for electron transfer should be the same. However, the charge transfer behavior is quite different among the three hybrids. In **Figure 6b**, polarization of the graphene substrate can be observed, but the isosurfaces on NiPc molecule is so tiny that the charge transfer through the interface is almost neglectable. In **Figure 6a**, we can see enhanced polarization of the NiPc-CN and graphene substrate, and the green isosurfaces corresponding to electron gain has a much larger size. NiPc-OMe does not have as large green isosurfaces as NiPc-CN, but they are more pronounced than

the pristine NiPc molecule. The major charge transfer happens at the region between the substituent groups and the substrate as can be seen in **Figure 6a** and **6c**, providing another evidence that the molecule/substrate interaction is substituent-dependent instead of the result of the electron push-pull effects.

To quantify the electron gain at the NiPc molecules from surface charging, we subtract the electron density of the neutral hybrid from the charged hybrid and project the electron density increases to Z direction (vertical to the graphene plane). Note that although a more sophisticated Poisson-Boltzmann model under grand canonical DFT scheme, which would require a symmetrizing slab, polarizable continuum, and a much thicker vacuum, is not employed due to extremely high computational cost with our already large model, the resulted error would be ~100 meV and is systematic.[68] The Z coordinate of graphene substrate is at 2.8 Angstrom, therefore the two large peaks of electron density above and below the Z=2.8 Angstrom indicate the majority of the extra electron are injected into the Π conjugate system of graphene. As the Z value increases, the electron density declines to around zero across the through-space region and then goes up at the position of NiPc molecules. Above the z position of zero flux at around 5.75 Angstrom, the smaller peak at around Z=6.2 Angstrom correspond to the electron that is successfully transferred to NiPc. By integrating the charge density across such region, the number of gained electron is quantitatively calculated to be 0.140, 0.081, and 0.104 |e| for the NiPc-CN, NiPc, and NiPc-OMe, respectively, indicating the order of charge transfer ability to be NiPc-CN@NC > NiPc-OMe@NC > NiPc@NC. Moreover, the charge transfer number correlates well with calculated adsorption energies linearly with R square of 0.9999 (**Figure S4**), establishing the adsorption energy of NiPc on substrate to be a viable descriptor of charge transfer kinetics at the $\pi - \pi$ stacking interface.

We would like to note that although vacuum model or implicit solvation model are used throughout the previous sections, we are fully aware of their limitations. From our primitive tests, including a micro-solvation of 8 explicit water molecules around the periphery of the NiPc-2H could lead to charge transfer of -0.16, -0.24, and +0.20 from the water to the NiPc-2H molecules for unsubstituted, -CN, and -OMe, respectively (Figure S5). The electron density differs from the isolated case not only near the peripheral rings

but also at the Ni-N$_4$ moiety, with the extent differing from substituent to substituent, thereby influencing the ground state redox properties. It has recently been reported that including a full realistic explicit solvation layer could alter the reaction energetics by a few hundred meV via hydrogen bonding stabilization, and it could even reveal alternative reaction pathways.[69] We are currently working to incorporate the explicit solvent environments, together with the substrate part that we are to discuss in the next section, into a unified realistic model for electrocatalysis.

Computational Screening. Sufficient insights into the substituent effects on the electronic structure of NiPc has been gained in the previous sections, and a few relationships are also discovered along the way, namely (i) more electron-rich metal center weakens CO adsorption to prevent poisoning, (ii) more electron-rich metal center strengthens Ni-N bond to protect integrity of Ni-N$_4$ moiety, (iii) lower LUMO energy level makes the reduction potential for activation of the NiPc molecule less negative, (iv) stronger interaction energy with substrate means facilitated charge transfer across the interface and ensures the immobilization. Inspired by the findings, we expand the scope to 42 types of substituents, with the full list provided in **Figure 7a**. To deal with the vast number of molecular permutations to explore in this rather large chemical space, we employ the recently developed SQM method GFN2-xTB to perform all the calculations in this section. The method is grounded quantum mechanically and has been benchmarked to predict geometry and molecular properties of with comparable accuracy to DFT.[57] In our tests, LUMO energy level calculated at GFN2-xTB linearly correlates with DFT result well with R square of 0.9999 (**Figure S6**). The geometry and RDG surfaces of NiPc interacting with substrate calculated at GFN2-xTB (Figure **S7**) are also consistent with the DFT results, proving that the NCI are correctly described. Although the substrate is modeled by a smaller aperiodic graphitic carbon sheet at GFN2-xTB instead of the periodic graphene model in previous DFT calculations, the interaction energy linearly correlates decently with R square of 0.9844 (**Figure S8**).

We begin with a dataset of symmetrically tetra- and octa- substituted NiPc molecules, i.e. substituting the site A or both site A and B with the same substituent, with a total number of 83 molecules. The Mulliken charge of Ni atom, the Mayer bond order of Ni-N, the

LUMO and HOMO energy levels of each molecule in the library are calculated after geometric optimization by SQM. It can be seen from **Figure 8a** that the Mulliken charge of Ni center is negatively correlated to the Mayer bond order of Ni-N, which echoes the previous finding that a more-electron rich Ni center strengthens the Ni-N bond. Therefore, the two aspects of long-term stability can be described by one variable, Mulliken charge of Ni center, to eliminate one degree of freedom. Since the atomic charge is related to the occupied orbitals, HOMO energy level usually correlates with atomic charge or oxidation state.[70] Unfortunately, on this symmetric dataset, the HOMO and LUMO energy levels are correlated. Since LUMO energy level has been shown to correlate with reduction potential, the molecular design comes to a dilemma where improving the stability would make the reduction potential more negative.

Recall that MO analysis indicates degenerate LUMO and LUMO+1 on symmetrically substituted NiPc molecules (**Figure S2**), asymmetric substitution is introduced to break the degeneracy to lower the LUMO energy levels without making as significant changes to HOMO energy levels. Since there are 42 different substituent including hydrogen and 8 substitution sites on NiPc, the chemical space would have size of c.a. 10 trillion molecules ($\sim 42^8$) which is beyond the capability of any brute-force exhaustion. Hence, we adopt a stochastic sampling to randomly introduce substituents on to the NiPc without any restriction on symmetry of number of different substituents, with a total size of 100,000 distinct molecules. After introducing asymmetric substitution, the LUMO and HOMO can be decoupled to some extent (**Figure 8b**), thereby making some room for optimization of performance beyond the scaling relation. Based on the understandings and the previously obtained correlations between calculated property and experimental values, we define a descriptor-based scheme to evaluate the overall performance of the substituted NiPc molecule. The descriptor of reduction potential of activation $\boldsymbol{D}_{\text{potential}}$ is defined as:

$$\boldsymbol{D}_{\text{potential}}(X) = \frac{\boldsymbol{E}_{\text{LUMO}}(\text{ref}) - \boldsymbol{E}_{\text{LUMO}}(X)}{|\boldsymbol{E}_{\text{LUMO}}(\text{ref})|} \times 100$$

The descriptor of long-term stability $\boldsymbol{D}_{\text{stability}}$ is defined as:

$$D_{\text{stabilty}}(X) = \frac{q_{\text{Ni}}(X) - q_{\text{Ni}}(\text{ref})}{|q_{\text{Ni}}(\text{ref})|} \times 100$$

Where the X is a substituted NiPc, the ref is the reference molecule, the E_{LUMO} and q_{Ni} are LUMO energy level and Mulliken charge of Ni center calculated by SQM, respectively. In this study, the reference molecule is chosen as NiPc-OMe since it is the highest-performance molecule in NiPc family that has been reported up to now. The $D_{\text{potential}}$ is plotted versus $D_{\text{stability}}$ on the symmetric and asymmetric dataset in **Figure 8d**. Despite the negative correlation between stability and potential, it is not a strict linear relationship. It is worth noting that in the symmetric dataset, no molecule that can outperform NiPc-OMe in both aspects (no black data points in first quartet), indicating it as the likely best candidate in this synthesis-friendly chemical subspace. On the asymmetric dataset, there are 572 molecules outperforming the reference molecule in terms of both stability and in potential, which is only 0.57% of all samples. Despite the excitement, one should be cautious since the asymmetric substitution can also lead to molecular structures that are sterically unfavorable for immobilization due to substituents sticking out-of-plane from steric repulsions, as can be seen in the peaks with positive adsorption energy in **Figure 8c**. This demonstrates the necessity to take into account the interaction with substrate in molecular design.

The best-performing molecules from stochastic sampling are definitely not the best in the whole chemical space of substituted NiPc since a dataset of 10^4 molecules is just a drop of water in ocean of 10^{12} molecules. Stochastic sampling allows uniform exploration of the chemical space, but it is inefficient in optimizing toward a specific property. On the other hand, the sheer size of data set makes even semiempirical methods extremely expensive. To explore the vast chemical space of asymmetrically substituted NiPc efficiently in an affordable way, we develop a GA searcher for global optimization of NiPc properties in the chemical space of substituent permutations and integrate NN models into the search. The workflow of the GA searcher and the architecture of the NN are shown in **Figure 7b** and **7c**, respectively. The NN is trained on the data-augmented stochastic sampled dataset with the one-hot encoded representation of the NiPc as input. The trained NN can achieve pretty accurate prediction of $D_{\text{potential}}$, $D_{\text{stability}}$, and E_{ads}

on the test set with R square of 0.9853, 0.9907, and 0.9990, respectively (**Figure S9**). Since the training set does not contain sufficient sampling of the outliers, especially in the direction of GA search, the validity of the NN-predicted value is checked against the SQM level results every 10 generations on-the-fly. The property calculation method is switched back to SQM after R square of the NN-predictions drop below 0.9, which indicates insufficient training of the NN model in this chemical subspace. Molecules with positive E_{ads} are removed in each generation to avoid misguiding of the search direction. For the candidates with a negative E_{ads}, the projection of ($D_{stability}$, $D_{overpot}$) to the normal vector (arrow in Figure 8f) of the fitted $D_{stability}$-$D_{overpot}$ linear correlation (dashed line in Figure 8f) is calculated, and the maximization of which is set as the search direction. Ten GA searches are performed with population size of 100, mutation rate of 33%, and convergence criterion of 50 generations. **Figure 8e** shows the results from one of the GA searches, and it can be seen that the population evolves from the diverse but ill-performing initial generation to higher-scoring populations gradually, and in the final population all the molecules outperform the reference molecules. The GA also has much improved efficiency from the stochastic search since the sampling of the ill-performing regions is avoided, with 42.90% of the sampled molecules outperforming reference molecules. In **Figure 8f**, we summarize the result from all ten GA searches and zoom in at the region of improved performance. The resulting molecules from GA greatly outperforms the ones from stochastic sampling by ~2 folds in $D_{potential}$ and by ~3 folds in $D_{stability}$. The final top 10 highest-scoring molecules are shown in **Figure 9**. The best candidate has slightly improved long-term stability and 0.46 eV stronger substrate interaction compared to the reference molecule. Its $D_{potential}$ is 5.44 which corresponds to a reduction potential of -0.59 V, being 100 mV less negative than the state-of-the-art NiPc-OMe. To verify the GA search results, DFT calculations are performed on the ten molecules at the same level of theory as in the previous section (Figure S10). All ten molecules show less negative reduction potentials, with the best among them (#8) outperforming the reference molecule NiPc-OMe by 110 mV. In terms of stability, four of them (#2,8,9,10) significantly outperform the reference molecule, while three of them (#1,5,6) show a small compromise in stability but still outperform the unsubstituted NiPc.

22

In summary, 7 of the 10 top-scoring molecules from the GA search are promising candidates for CO_2 reduction reaction.

Some designing strategies for NiPc can also be proposed base on the molecular structure of the search results: (i) introduce EDG to improve long-term stability, (ii) include different types of substituents with distinct electron push-pull effect to break the degeneracy of LUMO/LUMO+1 for a less negative reduction potential, (iii) a small number of strong EWG can be introduced to further break the degeneracy of LUMO and maximize the molecular polarizability for enhanced non-covalent interaction with substrate.

Conclusions

In summary, we studied the reaction mechanism of CO_2RR to CO on NiPc by DFT calculation, with an emphasis on the preceding reductive activation. The electronic structure and adsorption properties of the $Ni-N_4$ moiety, as well as how they are affected by substituents, are detailly investigated by analyzing molecular orbitals, generalized charge decomposition, electron density difference map, reduced density gradient map, electrostatic potential map, and symmetry adapted perturbation theory energy decomposition. The adsorption property and structural stability of the $Ni-N_4$ moiety is found to be related to electron density near the Ni center, therefore readily tunable by attaching EWG and EDG. The interaction between NiPc and the nanocarbon substrate is also investigated, and a correlation is discovered between the interaction energy and the charge transfer across the $\pi - \pi$ stacking interface. Such interaction strength is related to the polarizability of the molecule and the nature of the substituent instead of the electron push-pull effects on the $Ni-N_4$ moiety, opening up an additional dimension in molecular design. Finally, we developed a descriptor-based scheme for performance evaluation of the candidate molecule and screened through the chemical space of substituted NiPc using genetic algorithm search with semiempirical quantum mechanical calculations and predictive deep neural network models. Several promising molecules are identified with the best one outperforming the state-of-the-art reference molecule in stability and in reduction potential by 100 mV. Design strategies are proposed based on the top-down computational screening, and the workflow is highly generalizable and transferable to similar hybrid materials for various applications.
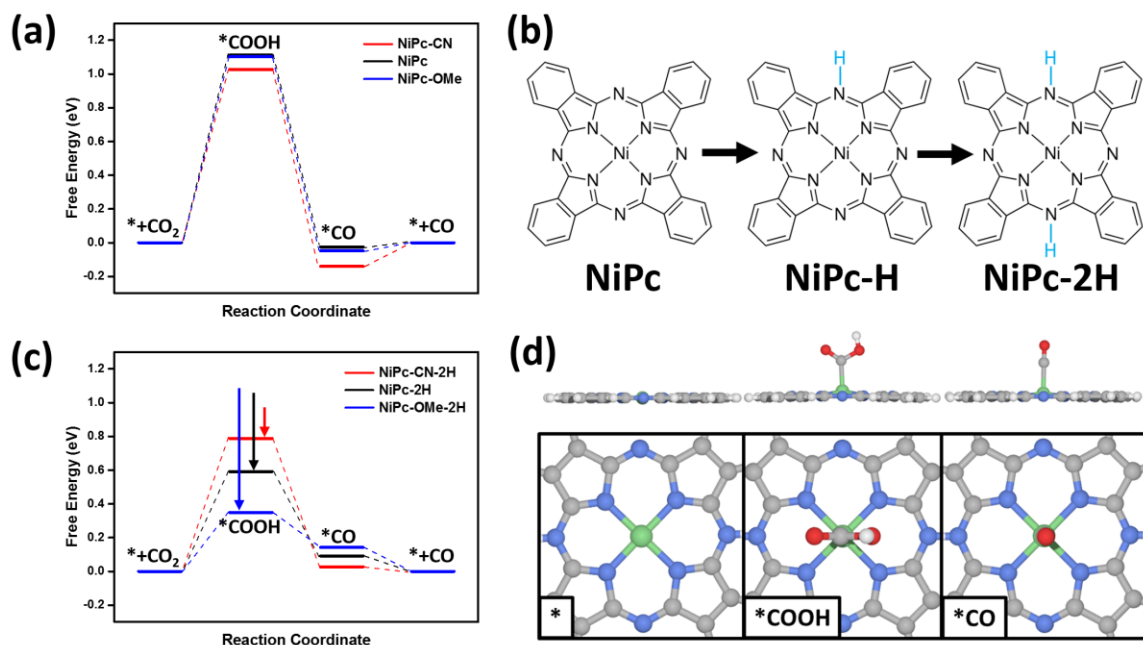
Figure 1. (a) The reaction profile of CO_2RR on NiPc, NiPc-CN, and NiPc-OMe. (b) The reductive activation process of NiPc. (c) The reaction profile of CO_2RR on NiPc-2H, NiPc-CN-2H, and NiPc-OMe-2H. (d) Optimized geometries of the three reaction intermediates, *, *COOH, and *CO, of CO_2RR on NiPc from top and side view. Color code: H – white, C – gray, N – blue, O – red, Ni – green.
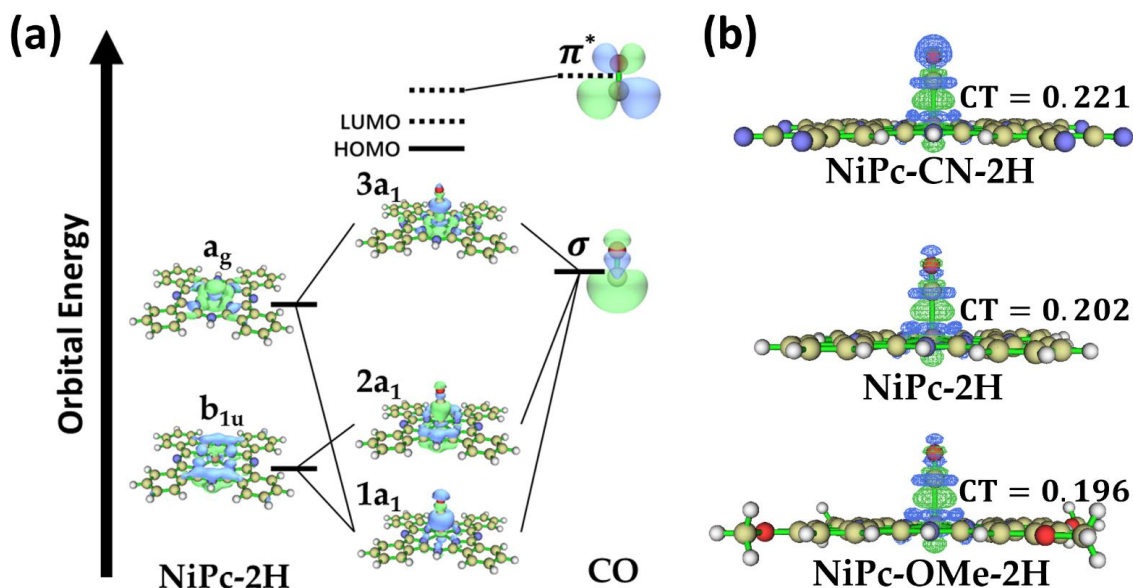
Figure 2. (a) The orbital interaction diagram of CO interacting with NiPc-2H from generalized charge decomposition analysis. Orbitals irrelevant with Ni-CO binding or has insignificant contribution from CO are not shown for clarity. (b) Electron density difference plot at isovalue = 0.001 showing electron transfer from CO to NiPc-CN-2H, NiPc-2H, and NiPc-OMe-2H, with green and blue lobes showing increase and decrease of electron density, respectively. Integrated charge transfer obtained from generalized charge decomposition analysis are labeled next to the corresponding structural models. Color code: H – white, C – tan, N – blue, O – red, Ni – green.
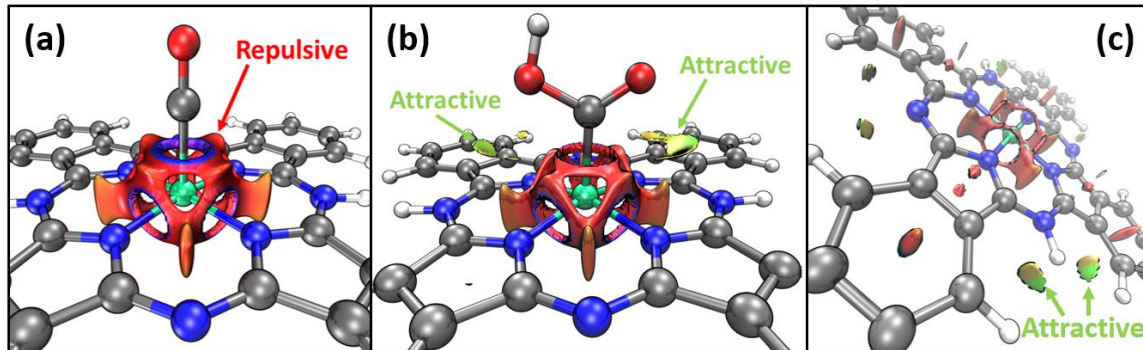
Figure 3. The reduced density gradient isosurfaces showing noncovalent interaction in (a) NiPc-2H*CO, (b) NiPc-2H*COOH, and (c) NiPc-2H. Red and green regions on isosurfaces correspond to repulsive and attractive noncovalent interactions, respectively. Color code: H – white, C – gray, N – blue, O – red, Ni – green.
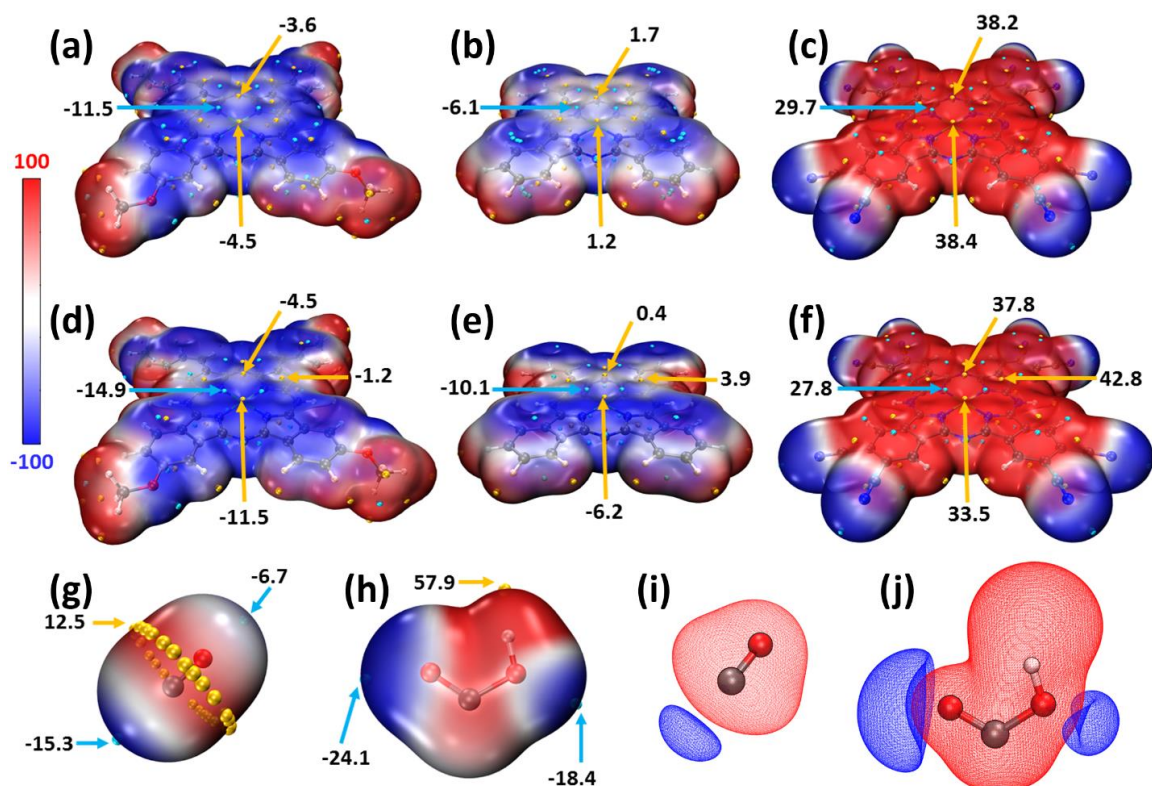
Figure 4. The electrostatic potential mapped van der Waals surface of (a) NiPc-CN, (b) NiPc, (c) NiPc-OMe, (d) NiPc-CN-2H, (e) NiPc-2H, (f) NiPc-OMe-2H, (g) CO fragment, and (h) COOH fragment. The electrostatic potential isosurfaces at 0.025 a.u. of (i) CO and (j) COOH fragments. Red and blue regions represent positive of negative electrostatic potential. Minima and maxima points are drawn as cyan and orange spheres, respectively. Unit of all labeled electrostatic potential values are kcal/mol. Color code: H – white, C – gray, N – blue, O – red, Ni – green.
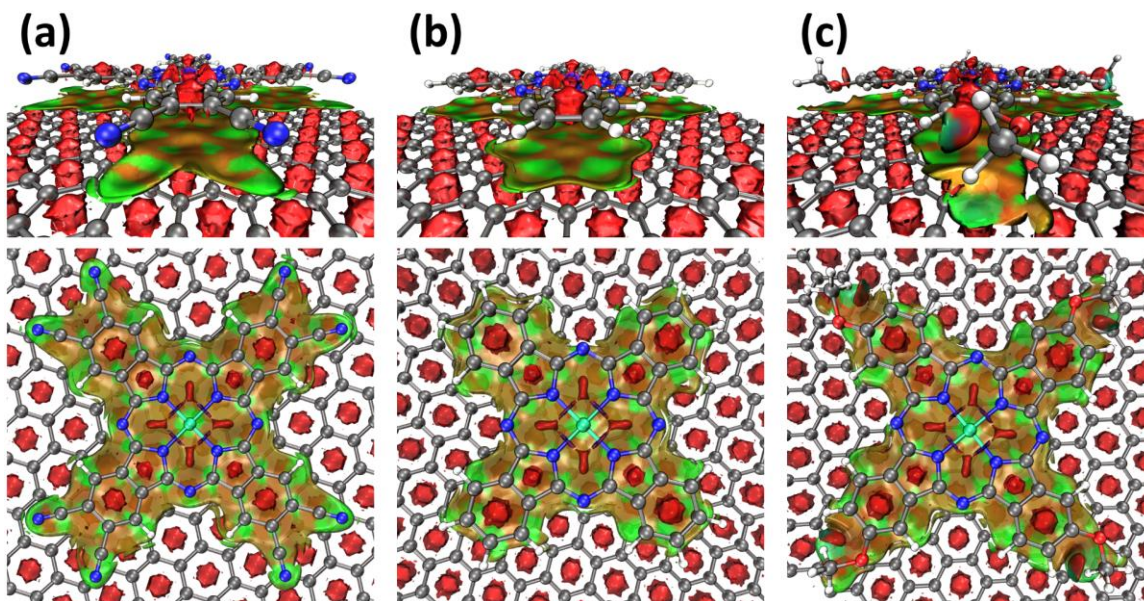
Figure 5. The reduced density gradient isosurfaces from promolecular density showing noncovalent interaction at the interface of (a) NiPc-CN@NC, (b) NiPc@NC, and (c) NiPc-OMe@NC. Red and green regions on isosurfaces correspond to repulsive and attractive noncovalent interactions, respectively. Color code: H – white, C – gray, N – blue, O – red, Ni – green.
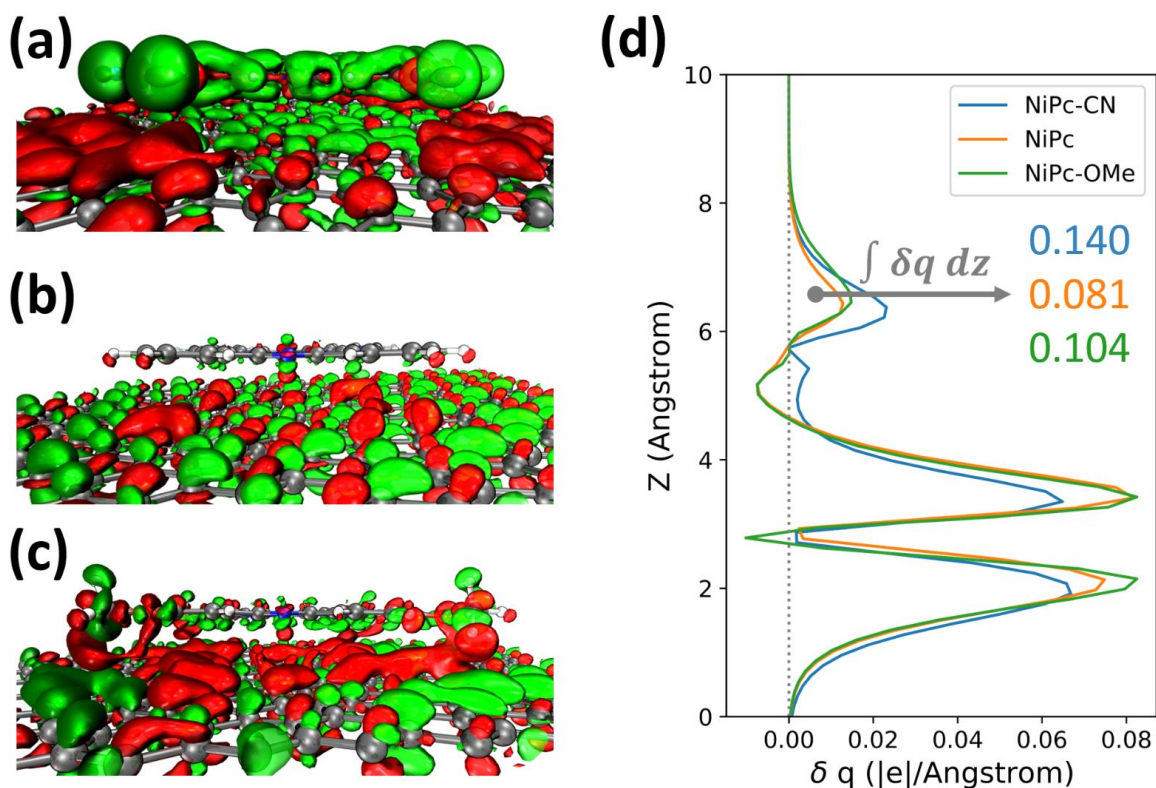
Figure 6. The electron density difference plot (isovalue=0.0025) showing charge transfer from a negatively charge graphene substrate to adsorbed (a) NiPc-CN, (b) NiPc, and (c) NiPc-OMe on graphene substrate. Green and red isosurfaces show increase or decrease of electron density, respectively. (d) The electron density difference after surface charging, projected to Z direction. The number of electrons gained by NiPc molecules from surface charging is calculated by integrating the charge density difference over the region around NiPc molecules, and the values are labeled in the plot.
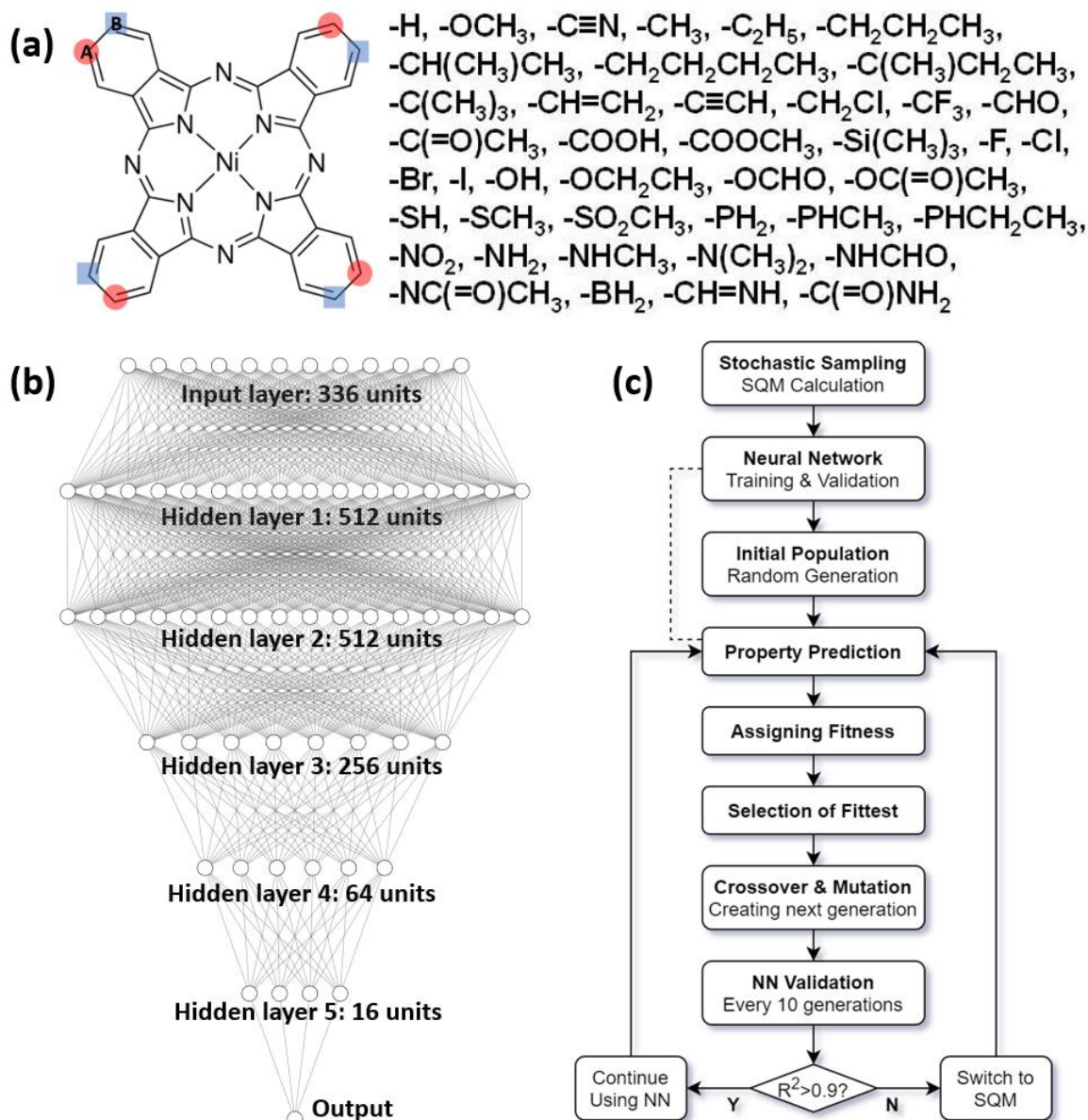
(a) -H, -OCH$_3$, -C≡N, -CH$_3$, -C$_2$H$_5$, -CH$_2$CH$_2$CH$_3$, -CH(CH$_3$)CH$_3$, -CH$_2$CH$_2$CH$_2$CH$_3$, -C(CH$_3$)CH$_2$CH$_3$, -C(CH$_3$)$_3$, -CH=CH$_2$, -C≡CH, -CH$_2$Cl, -CF$_3$, -CHO, -C(=O)CH$_3$, -COOH, -COOCH$_3$, -Si(CH$_3$)$_3$, -F, -Cl, -Br, -I, -OH, -OCH$_2$CH$_3$, -OCHO, -OC(=O)CH$_3$, -SH, -SCH$_3$, -SO$_2$CH$_3$, -PH$_2$, -PHCH$_3$, -PHCH$_2$CH$_3$, -NO$_2$, -NH$_2$, -NHCH$_3$, -N(CH$_3$)$_2$, -NHCHO, -NC(=O)CH$_3$, -BH$_2$, -CH=NH, -C(=O)NH$_2$

(b) Input layer: 336 units
Hidden layer 1: 512 units
Hidden layer 2: 512 units
Hidden layer 3: 256 units
Hidden layer 4: 64 units
Hidden layer 5: 16 units
Output

(c) Stochastic Sampling — SQM Calculation
Neural Network — Training & Validation
Initial Population — Random Generation
Property Prediction
Assigning Fitness
Selection of Fittest
Crossover & Mutation — Creating next generation
NN Validation — Every 10 generations
R^2>0.9? Y — Continue Using NN   N — Switch to SQM

Figure 7. (a) Structural formula of the NiPc with blue square and red circles labeling the peripheral sites where substituents are introduced, denoted as site A and site B, respectively. The full list of substituent scope is provided on the right. (b) The architecture of the deep neural network for property prediction in this study. (c) The general workflow of the genetic algorithm search.
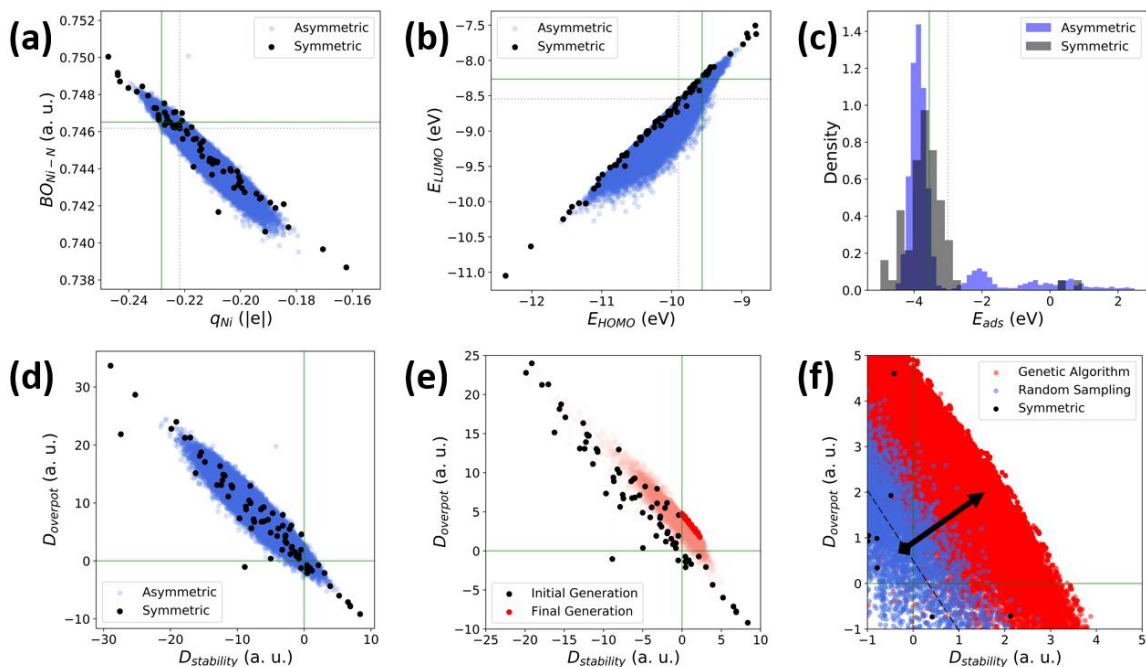
Figure 8. (a) Scatter plot of Mayer bond order of Ni-N versus atomic partial charge of Ni center of symmetrically and stochastically sampled asymmetrically substituted NiPc molecules. (b) Scatter plot of LUMO energy level versus HOMO energy level of symmetrically and stochastically sampled asymmetrically substituted NiPc molecules. (c) Histogram showing distribution of adsorption energies on graphene sheet of symmetrically and stochastically sampled asymmetrically substituted NiPc molecules. (d) Scatter plot of potential descriptor versus stability descriptor of symmetrically and stochastically sampled asymmetrically substituted NiPc molecules. (e) Scatter plot of potential descriptor versus stability descriptor on the trajectory of genetic algorithm search. (f) Scatter plot of potential descriptor versus stability descriptor of symmetrically and stochastically sampled asymmetrically substituted NiPc molecules, and trajectory of 10 independent GA searches. Gray dotted lines and green lines represent the values of NiPc and NiPc-OMe for reference. Dashed line and arrow in (f) represent the linear overpotential-stability correlation fitted on the stochastic dataset and the normal search direction.
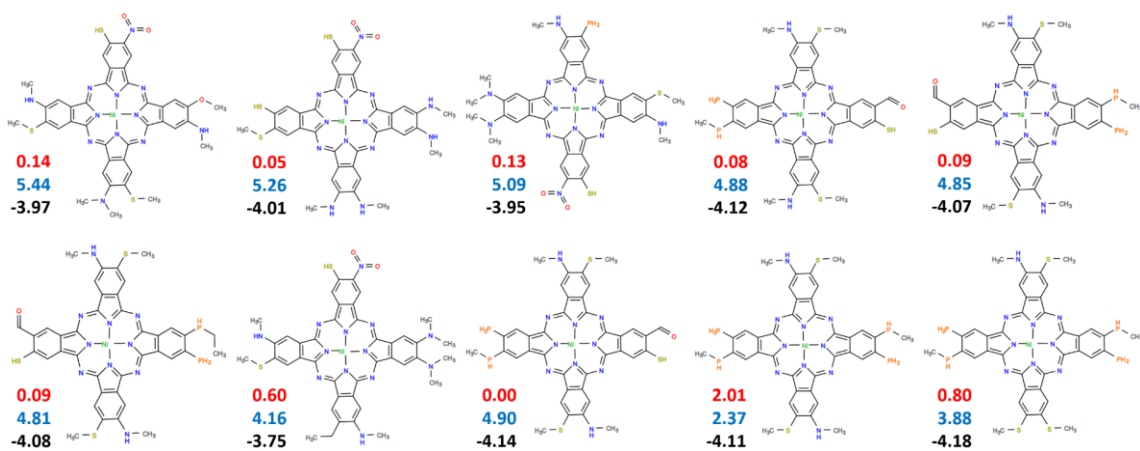
Figure 9. The structure of the top 10 substituted NiPc molecules with optimal performance from 10 independent genetic algorithm runs. The stability descriptor (top, in red), potential descriptor (middle, in blue), and adsorption energy on substrate in eV (bottom, in black) are labeled in the lower left of each molecule.

Table 1. SAPT energy decomposition results on NiPc-2H*CO, NiPc-CN-2H*CO, NiPc-OMe-2H*CO, NiPc-2H*COOH, NiPc-CN-2H*COOH, and NiPc-OMe-2H*COOH. All units are kcal/mol.

	$E_{\text{eletrostat}}$	E_{exchange}	$E_{\text{induction}}$	$E_{\text{dispersion}}$	E_{SAPT}
NiPc-CN-2H*CO	-51.89	83.59	-13.18	-12.65	5.87
NiPc-2H*CO	-55.17	88.26	-12.91	-13.03	7.16
NiPc-OMe-2H*CO	-55.65	88.96	-13.00	-13.11	7.20
NiPc-CN-2H*COOH	-35.52	79.12	-11.74	-18.87	12.99
NiPc-2H*COOH	-36.82	78.27	-21.65	-18.55	1.25
NiPc-OMe-2H*COOH	-36.73	78.06	-24.42	-18.54	-1.63

ASSOCIATED CONTENT

Supporting Information.

The following files are available free of charge.

Electron density map and color-filled cross section of the electron density increment of NiPc after reduction; Molecular orbital isosurfaces and energy levels of NiPc, NiPc-OMe, and NiPc-CN; Correlation plots; Reduced density gradient isosurfaces showing substrate interactions at GFN2-xTB; Validation of the trained machine learning models.

AUTHOR INFORMATION

Corresponding Author

*Corresponding Author's email: wangyg@sustech.edu.cn

Present Addresses

+ Department of Chemistry and Biochemistry, University of California, Los Angeles, 607 Charles E. Young Drive East, Los Angeles, California 90095, United States

Notes

The authors declare no competing financial interest.

The scripts for running genetic algorithm and deep neural network fitting, and the trained model .pkl files are available on: https://github.com/zishengz/molga-mpc

ACKNOWLEDGMENTS

Reference

(1)   Froelicher, T. L.; Paynter, D. J. Extending the Relationship between Global Warming and Cumulative Carbon Emissions to Multi-Millennial Timescales. *Environ. Res. Lett.* **2015**, *10* (7), 75002.

(2)   Seh, Z. W.; Kibsgaard, J.; Dickens, C. F.; Chorkendorff, I. B.; Nørskov, J. K.; Jaramillo, T. F. Combining Theory and Experiment in Electrocatalysis: Insights into Materials Design. *Science (80-.).* **2017**, *355* (6321), eaad4998.

(3)   Zhang, W.; Hu, Y.; Ma, L.; Zhu, G.; Wang, Y.; Xue, X.; Chen, R.; Yang, S.; Jin, Z. Progress and Perspective of Electrocatalytic CO_2 Reduction for Renewable Carbonaceous Fuels and Chemicals. *Adv. Sci.* **2018**, *5* (1), 1700275.

(4)   Jones, J.; Prakash, G. K. S.; Olah, G. A. Electrochemical CO_2 Reduction: Recent Advances and Current Trends. *Isr. J. Chem.* **2014**, *54* (10), 1451–1466.

(5)   Yang, X.-F.; Wang, A.; Qiao, B.; Li, J.; Liu, J.; Zhang, T. Single-Atom Catalysts: A New Frontier in Heterogeneous Catalysis. *Acc. Chem. Res.* **2013**, *46* (8), 1740–1748.

(6)   Wang, A.; Li, J.; Zhang, T. Heterogeneous Single-Atom Catalysis. *Nat. Rev. Chem.* **2018**, 1.

(7)   Zhu, C.; Fu, S.; Shi, Q.; Du, D.; Lin, Y. Single-atom Electrocatalysts. *Angew. Chemie Int. Ed.* **2017**, *56* (45), 13944–13960.

(8)   Li, X.; Wang, H.; Yang, H.; Cai, W.; Liu, S.; Liu, B. In Situ/Operando Characterization Techniques to Probe the Electrochemical Reactions for Energy Conversion. *Small Methods* **2018**, *2* (6), 1700395.

(9)   Su, X.; Yang, X.-F.; Huang, Y.; Liu, B.; Zhang, T. Single-Atom Catalysis toward Efficient CO_2 Conversion to CO and Formate Products. *Acc. Chem. Res.* **2018**, *52* (3), 656–664.

(10)   Chen, Y.; Yu, G.; Chen, W.; Liu, Y.; Li, G.-D.; Zhu, P.; Tao, Q.; Li, Q.; Liu, J.; Shen, X.; Li, H.; Huang, X.; Wang, D.; Asefa, T.; Zou, X. Highly Active, Nonprecious Electrocatalyst Comprising Borophene Subunits for the Hydrogen Evolution Reaction. *J. Am. Chem. Soc.* **2017**, *139* (36), 12370–12373. https://doi.org/10.1021/jacs.7b06337.

(11)   Yang, H. Bin; Hung, S.-F.; Liu, S.; Yuan, K.; Miao, S.; Zhang, L.; Huang, X.; Wang, H.-Y.; Cai, W.; Chen, R. Atomically Dispersed Ni (I) as the Active Site for Electrochemical CO_2 Reduction. *Nat. Energy* **2018**, *3* (2), 140–147.

(12)   Sun, T.; Xu, L.; Wang, D.; Li, Y. Metal Organic Frameworks Derived Single Atom Catalysts for Electrocatalytic Energy Conversion. *Nano Res.* **2019**, 1–14.

(13) Lee, L. K.; Sabelli, N. H.; LeBreton, P. R. Theoretical Characterization of Phthalocyanine, Tetraazaporphyrin, Tetrabenzoporphyrin, and Porphyrin Electronic Spectra. *J. Phys. Chem.* **1982**, *86* (20), 3926–3931.

(14) Marom, N.; Kronik, L. Density Functional Theory of Transition Metal Phthalocyanines, I: Electronic Structure of NiPc and CoPc—Self-Interaction Effects. *Appl. Phys. A* **2009**, *95* (1), 159–163.

(15) Drexler, K. E. Molecular Engineering: An Approach to the Development of General Capabilities for Molecular Manipulation. *Proc. Natl. Acad. Sci.* **1981**, *78* (9), 5275–5278.

(16) Solis, B. H.; Hammes-Schiffer, S. Proton-Coupled Electron Transfer in Molecular Electrocatalysis: Theoretical Methods and Design Principles. *Inorg. Chem.* **2014**, *53* (13), 6427–6443.

(17) Klug, C. M.; Cardenas, A. J. P.; Bullock, R. M.; O'Hagan, M.; Wiedner, E. S. Reversing the Tradeoff between Rate and Overpotential in Molecular Electrocatalysts for H2 Production. *ACS Catal.* **2018**, *8* (4), 3286–3296.

(18) Costentin, C.; Savéant, J.-M. Towards an Intelligent Design of Molecular Electrocatalysts. *Nat. Rev. Chem.* **2017**, *1* (11), 1–8.

(19) Mathew, S.; Yella, A.; Gao, P.; Humphry-Baker, R.; Curchod, B. F. E.; Ashari-Astani, N.; Tavernelli, I.; Rothlisberger, U.; Nazeeruddin, M. K.; Grätzel, M. Dye-Sensitized Solar Cells with 13% Efficiency Achieved through the Molecular Engineering of Porphyrin Sensitizers. *Nat. Chem.* **2014**, *6* (3), 242.

(20) Ding, Y.; Zhang, C.; Zhang, L.; Zhou, Y.; Yu, G. Molecular Engineering of Organic Electroactive Materials for Redox Flow Batteries. *Chem. Soc. Rev.* **2018**, *47* (1), 69–103.

(21) Yang, C.; Ma, B. C.; Zhang, L.; Lin, S.; Ghasimi, S.; Landfester, K.; Zhang, K. A. I.; Wang, X. Molecular Engineering of Conjugated Polybenzothiadiazoles for Enhanced Hydrogen Production by Photosynthesis. *Angew. Chemie Int. Ed.* **2016**, *55* (32), 9202–9206.

(22) Sieh, D.; Lacy, D. C.; Peters, J. C.; Kubiak, C. P. Reduction of CO2 by Pyridine Monoimine Molybdenum Carbonyl Complexes: Cooperative Metal–Ligand Binding of CO2. *Chem. Eur. J.* **2015**, *21* (23), 8497–8503.

(23) Dey, S.; Mondal, B.; Chatterjee, S.; Rana, A.; Amanullah, S. K.; Dey, A. Molecular Electrocatalysts for the Oxygen Reduction Reaction. *Nat. Rev. Chem.* **2017**, *1* (12), 98.

(24) Zhang, Z.; Yang, T.; Qin, P.; Dang, L. Nickel Bis (Dithiolene) Complexes for Electrocatalytic Hydrogen Evolution: A Computational Study. *J. Organomet. Chem.* **2018**, *864*, 143–147.

(25)   Koerstz, M.; Christensen, A. S.; Mikkelsen, K. V; Nielsen, M. B.; Jensen, J. H. High Throughput Virtual Screening of 230 Billion Molecular Solar Heat Battery Candidates. *PeerJ Phys. Chem.* **2021**, *3*, e16.

(26)   Sanchez-Lengeling, B.; Aspuru-Guzik, A. Inverse Molecular Design Using Machine Learning: Generative Models for Matter Engineering. *Science (80-.).* **2018**, *361* (6400), 360–365.

(27)   Schreier, M.; Luo, J.; Gao, P.; Moehl, T.; Mayer, M. T.; Grätzel, M. Covalent Immobilization of a Molecular Catalyst on Cu2O Photocathodes for CO2 Reduction. *J. Am. Chem. Soc.* **2016**, *138* (6), 1938–1946.

(28)   Wang, J.; Gan, L.; Zhang, Q.; Reddu, V.; Peng, Y.; Liu, Z.; Xia, X.; Wang, C.; Wang, X. A Water-Soluble Cu Complex as Molecular Catalyst for Electrocatalytic CO2 Reduction on Graphene-Based Electrodes. *Adv. Energy Mater.* **2019**, *9* (3), 1803151.

(29)   Li, X.; Liu, L.; Ren, X.; Gao, J.; Huang, Y.; Liu, B. Microenvironment Modulation of Single-Atom Catalysts and Their Roles in Electrochemical Energy Conversion. *Sci. Adv.* **2020**, *6* (39), eabb6833. https://doi.org/10.1126/sciadv.abb6833.

(30)   Sun, L.; Reddu, V.; Fisher, A. C.; Wang, X. Electrocatalytic Reduction of Carbon Dioxide: Opportunities with Heterogeneous Molecular Catalysts. *Energy Environ. Sci.* **2020**, *13* (2), 374–403.

(31)   Zhang, X.; Wu, Z.; Zhang, X.; Li, L.; Li, Y.; Xu, H.; Li, X.; Yu, X.; Zhang, Z.; Liang, Y. Highly Selective and Active CO 2 Reduction Electrocatalysts Based on Cobalt Phthalocyanine/Carbon Nanotube Hybrid Structures. *Nat. Commun.* **2017**, *8*, 14675.

(32)   Xiao Zhang, Yang Wang, Meng Gu, Maoyu Wang, Zisheng Zhang, Weiying Pan, Zhan Jiang, Hailiang Wang, George E. Sterbinsky, Yang-Gang Wang, Zhenxing Feng, Yongye Liang, Jun Li, H. D. Molecular Engineering of Dispersed Electrocatalysts on Carbon Nanotubes for Selective CO2 Reduction. *Submitted*.

(33)   Liu, S.; Yang, H. Bin; Hung, S.; Ding, J.; Cai, W.; Liu, L.; Gao, J.; Li, X.; Ren, X.; Kuang, Z. Elucidating the Electrocatalytic CO2 Reduction Reaction over a Model Single-Atom Nickel Catalyst. *Angew. Chemie Int. Ed.* **2020**, *59* (2), 798–803.

(34)   Wu, Y.; Jiang, Z.; Lu, X.; Liang, Y.; Wang, H. Domino Electroreduction of CO2 to Methanol on a Molecular Catalyst. *Nature* **2019**, *575* (7784), 639–642. https://doi.org/10.1038/s41586-019-1760-8.

(35)   Peterson, A. A.; Abild-Pedersen, F.; Studt, F.; Rossmeisl, J.; Nørskov, J. K. How Copper Catalyzes the Electroreduction of Carbon Dioxide into Hydrocarbon Fuels. *Energy Environ. Sci.* **2010**, *3* (9), 1311–1315.

(36)   Frisch, M. J. No Title. et al. Gaussian 09, Gaussian, Inc., Wallingford CT.

(37)   Adamo, C.; Barone, V. Toward Reliable Density Functional Methods without Adjustable Parameters: The PBE0 Model. *J. Chem. Phys.* **1999**, *110* (13), 6158–6170. https://doi.org/10.1063/1.478522.

(38)   Grimme, S.; Ehrlich, S.; Goerigk, L. Effect of the Damping Function in Dispersion Corrected Density Functional Theory. *J. Comput. Chem.* **2011**, *32* (7), 1456–1465.

(39)   Andrae, D.; Häußermann, U.; Dolg, M.; Stoll, H.; Preuß, H. Energy-Adjustedab Initio Pseudopotentials for the Second and Third Row Transition Elements. *Theor. Chim. Acta* **1990**, *77* (2), 123–141. https://doi.org/10.1007/BF01114537.

(40)   Hariharan, P. C.; Pople, J. A. The Influence of Polarization Functions on Molecular Orbital Hydrogenation Energies. *Theor. Chim. Acta* **1973**, *28* (3), 213–222.

(41)   Gordon, M. S. The Isomers of Silacyclopropane. *Chem. Phys. Lett.* **1980**, *76* (1), 163–168.

(42)   Binning, R. C.; Curtiss, L. A. Compact Contracted Basis Sets for Third-row Atoms: Ga–Kr. *J. Comput. Chem.* **1990**, *11* (10), 1206–1216.

(43)   Marenich, A. V; Cramer, C. J.; Truhlar, D. G. Universal Solvation Model Based on Solute Electron Density and on a Continuum Model of the Solvent Defined by the Bulk Dielectric Constant and Atomic Surface Tensions. *J. Phys. Chem. B* **2009**, *113* (18), 6378–6396. https://doi.org/10.1021/jp810292n.

(44)   Zhao, Y.; Schultz, N. E.; Truhlar, D. G. Design of Density Functionals by Combining the Method of Constraint Satisfaction with Parametrization for Thermochemistry, Thermochemical Kinetics, and Noncovalent Interactions. *J. Chem. Theory Comput.* **2006**, *2* (2), 364–382.

(45)   Ho, J.; Klamt, A.; Coote, M. L. Comment on the Correct Use of Continuum Solvent Models. *J. Phys. Chem. A* **2010**, *114* (51), 13442–13444.

(46)   Lu, T.; Chen, F. Multiwfn: A Multifunctional Wavefunction Analyzer. *J. Comput. Chem.* **2012**, *33* (5), 580–592.

(47)   Jeziorski, B.; Moszynski, R.; Szalewicz, K. Perturbation Theory Approach to Intermolecular Potential Energy Surfaces of van Der Waals Complexes. *Chem. Rev.* **1994**, *94* (7), 1887–1930. https://doi.org/10.1021/cr00031a008.

(48)   Turney, J. M.; Simmonett, A. C.; Parrish, R. M.; Hohenstein, E. G.; Evangelista, F. A.; Fermann, J. T.; Mintz, B. J.; Burns, L. A.; Wilke, J. J.; Abrams, M. L.; Russ, N. J.; Leininger, M. L.; Janssen, C. L.; Seidl, E. T.; Allen, W. D.; Schaefer, H. F.; King, R. A.; Valeev, E. F.; Sherrill, C. D.; Crawford, T. D. Psi4: An Open-Source Ab Initio Electronic Structure Program. *Wiley Interdiscip. Rev. Comput. Mol. Sci.* **2012**, *2* (4), 556–565.

https://doi.org/10.1002/wcms.93.

(49)   Dunning Jr, T. H. Gaussian Basis Sets for Use in Correlated Molecular Calculations. I.
         The Atoms Boron through Neon and Hydrogen. *J. Chem. Phys.* **1989**, *90* (2), 1007–1023.

(50)   VandeVondele, J.; Krack, M.; Mohamed, F.; Parrinello, M.; Chassaing, T.; Hutter, J.
         Quickstep: Fast and Accurate Density Functional Calculations Using a Mixed Gaussian
         and Plane Waves Approach. *Comput. Phys. Commun.* **2005**, *167* (2), 103–128.

(51)   VandeVondele, J.; Hutter, J. Gaussian Basis Sets for Accurate Calculations on Molecular
         Systems in Gas and Condensed Phases. *J. Chem. Phys.* **2007**, *127* (11), 114105.
         https://doi.org/10.1063/1.2770708.

(52)   Lippert, B. G.; Parrinello, J. H.; Michele. A Hybrid Gaussian and Plane Wave Density
         Functional Scheme. *Mol. Phys.* **1997**, *92* (3), 477–488.
         https://doi.org/10.1080/002689797170220.

(53)   Ishii, A.; Yamamoto, M.; Asano, H.; Fujiwara, K. DFT Calculation for Adatom
         Adsorption on Graphene Sheet as a Prototype of Carbon Nanotube Functionalization. *J.
         Phys. Conf. Ser.* **2008**, *100* (5), 52087. https://doi.org/10.1088/1742-6596/100/5/052087.

(54)   Umadevi, D.; Sastry, G. N. Quantum Mechanical Study of Physisorption of Nucleobases
         on Carbon Materials: Graphene versus Carbon Nanotubes. *J. Phys. Chem. Lett.* **2011**, *2*
         (13), 1572–1576.

(55)   Grimme, S. Density Functional Theory with London Dispersion Corrections. *Wiley
         Interdiscip. Rev. Comput. Mol. Sci.* **2011**, *1* (2), 211–228.

(56)   Grimme, S. XTB, a Tight-Binding Quantum Chemistry Code for Large Molecules. *Univ.
         Bonn* **2019**.

(57)   Bannwarth, C.; Ehlert, S.; Grimme, S. GFN2-XTB—An Accurate and Broadly
         Parametrized Self-Consistent Tight-Binding Quantum Chemical Method with Multipole
         Electrostatics and Density-Dependent Dispersion Contributions. *J. Chem. Theory Comput.*
         2019, *15* (3), 1652–1671.

(58)   Weininger, D. SMILES, a Chemical Language and Information System. 1. Introduction to
         Methodology and Encoding Rules. *J. Chem. Inf. Comput. Sci.* **1988**, *28* (1), 31–36.

(59)   O'Boyle, N. M.; Banck, M.; James, C. A.; Morley, C.; Vandermeersch, T.; Hutchison, G.
         R. Open Babel: An Open Chemical Toolbox. *J. Cheminform.* **2011**, *3* (1), 33.

(60)   Yoshikawa, N.; Hutchison, G. R. Fast, Efficient Fragment-Based Coordinate Generation
         for Open Babel. *J. Cheminform.* **2019**, *11* (1), 49. https://doi.org/10.1186/s13321-019-
         0372-5.

(61)   Kapusta, S.; Hackerman, N. Carbon Dioxide Reduction at a Metal Phthalocyanine

Catalyzed Carbon Electrode. *J. Electrochem. Soc.* **1984**, *131* (7), 1511.

(62) Zhang, X.; Wang, Y.; Gu, M.; Wang, M.; Zhang, Z.; Pan, W.; Jiang, Z.; Zheng, H.; Lucero, M.; Wang, H. Molecular Engineering of Dispersed Nickel Phthalocyanines on Carbon Nanotubes for Selective CO 2 Reduction. *Nat. Energy* **2020**, *5* (9), 684–692.

(63) Dong, Q.; Zhang, X.; He, D.; Lang, C.; Wang, D. Role of H2O in CO2 Electrochemical Reduction As Studied in a Water-in-Salt System. *ACS Cent. Sci.* **2019**, *5* (8), 1461–1467. https://doi.org/10.1021/acscentsci.9b00519.

(64) Zagal, J. H.; Gulppi, M. A.; Cárdenas-Jirón, G. Metal-Centered Redox Chemistry of Substituted Cobalt Phthalocyanines Adsorbed on Graphite and Correlations with MO Calculations and Hammett Parameters. Electrocatalytic Reduction of a Disulfide. *Polyhedron* **2000**, *19* (22), 2255–2260. https://doi.org/https://doi.org/10.1016/S0277-5387(00)00486-1.

(65) Zagal, J. H.; Cárdenas-Jirón, G. I. Reactivity of Immobilized Cobalt Phthalocyanines for the Electroreduction of Molecular Oxygen in Terms of Molecular Hardness. *J. Electroanal. Chem.* **2000**, *489* (1), 96–100. https://doi.org/https://doi.org/10.1016/S0022-0728(00)00209-6.

(66) Méndez-Hernández, D. D.; Tarakeshwar, P.; Gust, D.; Moore, T. A.; Moore, A. L.; Mujica, V. Simple and Accurate Correlation of Experimental Redox Potentials and DFT-Calculated HOMO/LUMO Energies of Polycyclic Aromatic Hydrocarbons. *J. Mol. Model.* **2013**, *19* (7), 2845–2848. https://doi.org/10.1007/s00894-012-1694-7.

(67) Sinnokrot, M. O.; Sherrill, C. D. Substituent Effects in Π−π Interactions: Sandwich and T-Shaped Configurations. *J. Am. Chem. Soc.* **2004**, *126* (24), 7690–7697. https://doi.org/10.1021/ja049434a.

(68) Steinmann, S. N.; Sautet, P. Assessing a First-Principles Model of an Electrochemical Interface by Comparison with Experiment. *J. Phys. Chem. C* **2016**, *120* (10), 5619–5623. https://doi.org/10.1021/acs.jpcc.6b01938.

(69) Cao, H.; Xia, G.-J.; Chen, J.-W.; Yan, H.-M.; Huang, Z.; Wang, Y.-G. Mechanistic Insight into the Oxygen Reduction Reaction on the Mn–N4/C Single-Atom Catalyst: The Role of the Solvent Environment. *J. Phys. Chem. C* **2020**, *124* (13), 7287–7294.

(70) Dance, I. The Correlation of Redox Potential, HOMO Energy, and Oxidation State in Metal Sulfide Clusters and Its Application to Determine the Redox Level of the FeMo-Co Active-Site Cluster of Nitrogenase. *Inorg. Chem.* **2006**, *45* (13), 5084–5091. https://doi.org/10.1021/ic060438l.